Nanoscale

Morphology-induced dielectric enhancement in polymer nanocomposites

Journal:	*Nanoscale*
Manuscript ID	NR-ART-01-2021-000165.R1
Article Type:	Paper
Date Submitted by the Author:	18-May-2021
Complete List of Authors:	Zhang, Bing; North Carolina State University, Physics Chen, Xin; penn state university, materials science & engineering Lu, Wenchang; North Carolina State University, Physics Zhang, Qiming; The Pennsylvania State University, Electrical Engineering Bernholc, Jerry; North Carolina State University, Physics; NC State University

Morphology-induced dielectric enhancement in polymer nanocomposites

Bing Zhang,[1] Xin Chen,[3] Wenchang Lu,[1,2] Q.M. Zhang,[3] and J. Bernholc[1]
[1]Department of Physics, North Carolina State University, Raleigh, NC 27695-8202, USA
[2]Computional Sciences and Engineering Division, Oak Ridge National Laboratory, Oak Ridge, TN 37831, USA
[3]Materials Research Institute and Department of Materials Science and Engineering, The Pennsylvania State University, University Park, Pennsylvania 16802, USA

Abstract: The mechanism of the recently discovered enhancement of dielectric properties in dilute polymer-nanoparticle composites is investigated by experiments and computer simulations. We show that the weakening of the hydrogen bonds between the nanoparticles and the polymer chains reduces the polymer-nanoparticle composite's dielectric enhancement. The subsequent multiscale simulations investigate the attachment of solvated highly dipolar polymers to oxide nanoparticles, which leads to deposition of nanoparticle-polymer blobs during solution casting and a reduced density compared to a neat polymer film. Coarse-grained simulations of nanocomposite morphology are followed by molecular dynamics and density functional theory calculations of permittivities. The increased free volume in the nanocomposite enables easier reorientation of monomer dipoles with an applied electric field, and thus a higher dielectric permittivity. The numerical results are in excellent agreement with experimental data for PEEU and PEI nanocomposites.

I. INTRODUCTION

The well-known Ragone plots [1] relate electric energy storage density and power density. Conventional batteries have very high energy densities but low power densities. Capacitors, on the other hand, have low energy densities but the highest power densities and can fully charge and discharge over tens of milliseconds. Furthermore, in contrast to batteries, capacitors can survive millions of charge and discharge cycles. Dielectrics are critical for the design of high-performance capacitors because the energy density U stored in the capacitor is

$$U = \frac{1}{8\pi} K E_b^2, \tag{1}$$

where K is the relative permittivity, and E_b is the breakdown field strength. The permittivity is thus critical to attaining high energy density of capacitors. Polymers are usually the preferred dielectrics for high-performance capacitors because of their high breakdown voltages, gentle failure, and the easy manufacturing of flexible dielectric films. However, the best currently used dielectric material, biaxially oriented polypropylene (BOPP) has a permittivity of 2.2 [2,3]. Many research programs have been devoted to increasing the effective permittivity of polymer dielectrics to increase the stored energy. The research avenues include storing electrical energy through a reversible, electric-field-induced phase transition from a non-polar to a polar structure [4–7], an admixture of a significant amount of high-K dielectric powders, such as barium titanate

[8,9], and use of polymers with high permittivities due to monomers with strongly dipolar units [10–13]. The latter polymers are "linear" dielectrics with constant permittivities whose values do not change with the electric field so that the stored energy depends quadratically on the electric field and reaches the maximum at the breakdown field. However, it has recently been discovered that it is possible to increase a linear polymer dielectric's permittivity significantly by special processing. Refs. [11,12] noted that non-crystalline polymer films with substantial disorder have dramatically larger permittivities than ordered semi-crystalline structures. The authors attributed this enhancement to an increase in volume, which introduces additional free volume. The extra volume weakens steric constraints and allows the monomer dipoles to rotate and align better with the applied field, thereby increasing permittivity. For example, a crystalline poly(arylene ether urea) (PEEU) powder has a permittivity of 3.65, while the permittivity of a disordered PEEU film is 4.7 [11]. The increased free volume concept was exploited again by blending two dissimilar polymers, such as PEEU (K = 4.7) and aromatic polythiourea (ArPTU, K = 4.4). The resulting structural frustration increased the free volume and led to permittivity, reaching 7.5 [14]. A computational design of organic polymer dielectrics via computational screening with targeted experimental synthesis was advocated by Ref. [15]. Several potential candidates have been identified, which are being evaluated experimentally.

Recently, a novel way to increase permittivity in highly dipolar polymers was discovered [16,17]. Addition of an ultralow (<1 vol%) concentration of small diameter filler nanoparticles of, e.g., Al_2O_3(20 nm size) increased the permittivity of PEEU from 4.7 to 7.4, and that of polyetherimide (PEI) from 3.2 to 5.0. At these ultralow filler concentrations, the dramatic permittivity increase cannot be explained by permittivity contributions from the nanoparticles and must be due to different morphology of the nanocomposite than that of the pure polymer.

In the original article [16] an empirical model was developed, which assumed a non-uniform permittivity around each nanoparticle of the form

$$K(r) = K_0 + [Ag - B]e^{-g}, \tag{2}$$

where K_0 is the permittivity of the polymer matrix, r is the distance from the surface of the nanoparticle, $g = \left(\frac{r}{r_0}\right)^2$, and r_0, A and B are fitting constants. This model was able to reproduce qualitatively the nanocomposite data for different nanoparticle diameters and concentrations. However, The model does not provide any information about the nanocomposite's structural changes or the origin of the dielectric enhancement. There were studies showing that the hydroxy groups on the nanoparticles respond to the microwave band, change the bandgaps and therefore affect the electronic polarizability and mobility. [18–21] However, with the tiny amount of nanoparticles, the dielectric enhancement cannot be explained by contributions from the hydroxy groups. A theoretical study [22] investigated the dielectric properties of polymer chains attached to an Al_2O_3 surface and showed that in an interfacial region of 15-55 Å away from the surface, the permittivity is significantly enhanced. Nevertheless, an interfacial region of this thickness cannot, by itself, explain a ~50% increase of permittivity of the entire film.

This work describes the results of an extensive experimental-computational investigation of polymer nanocomposites, focusing on nanoparticle-induced morphology changes and the associated changes in permittivity. In experiments, we observe that by weakening the hydrogen bonds between nanoparticles and the polymer, the dielectric constant enhancement is diminished. Accordingly, we assume that the polymer chains attach to nanoparticles in solution. Coarse-

grained simulations model the nanoparticle-polymer blobs and their aggregation to establish the nanocomposite morphology. They are followed by all-atom simulations to extract the dipolar and ionic contribution to permittivity, and density functional theory calculations to obtain the electronic part. The combined results show how a dilute concentration of nanoparticles in solution-cast films leads to polymer density variations that enhance permittivity in accordance with the experimental results. The paper is organized as follows. Section II describes the Experimental Methods and Results, Section III the Computational Model and Methodology, Section IV presents the Computational Results and Discussion, while Section V contains the Summary and Conclusions.

II. EXPERIMENTAL METHODS AND RESULTS

In the prior experiments [16,17], the nanocomposite films were prepared by solution casting, solvating polymer resin and oxide nanoparticles in either dimethylformamide or dimethylacetamide. The solution was cast on a glass slide, and the solvent was evaporated at high temperature in a drying oven. The resulting nanocomposite films' permittivities peak at very low volume% of nanoparticles, ranging from ~0.2% for 5 nm particles to ~0.8% for 50 nm nanoparticles. The chemical nature of the nanoparticles, Al_2O_3, MgO, SiO_2, BN, or $BaTiO_3$, has a minimal effect on the enhancement. Nanocomposite's permittivity with smaller nanoparticles, which have a greater surface to volume ratio than larger nanoparticles, peaks at lower volume% than for larger nanoparticles. We thus focus on the interface between the nanoparticles and the polymer. To diminish the possibility of hydrogen bonding between the alumina nanoparticles and polymer, we make hydrogen-bond-weakened PEI and PEEU nanocomposites by admixing surface-modified alumina nanoparticles, in which the alumina nanoparticle surfaces are partially coated by strongly bonded organic molecules, significantly reducing their propensity for hydrogen bonding.

IIA. Surface modification of alumina nanoparticles

Al_2O_3 nanoparticles were added in a flask with anhydrous toluene and then stirred in ultrasonic bath for two hours to disperse the nanoparticles. Ethyltrimethoxysilane (from Sigma-Aldrich) was then added to the solution and magnetically stirred for one hour. The whole system was placed in a silicone oil bath and heated up to 85 ˚C, refluxing the condensate for 24 hours under N_2 atmosphere. The modified particles were collected and dried in a vacuum oven at 80 ˚C.

IIB. PEI and PEEU Composites films fabrication

We fabricated PEI nanocomposites with Alumina nanofillers (neat or modified) with various filler loadings. Al_2O_3 nanoparticles with diameter of 20 nm were purchased from US Nano. ULTEM 1000 PEI polymer resin was provided by PolyK (State College). The composite films were prepared by solution casting method. To prepare the nanocomposite solution, a proper amount of PEI powder was dissolved in dimethylformamide (DMF) at 80 ˚C and stirred overnight to obtain a homogeneous solution. Nanofillers with a given amount corresponding to each volume content were dispersed in DMF at room temperature using an Elma "P" Series Ultrasonics (250 W) for 1 hr. Afterward, the PEI solution was poured into this suspension and sonicated for 12 hrs. The solution was then cast onto a clean glass slide. The solution-cast films were kept in a drying oven at 70 ˚C for 12 hours to remove the solvent and then heated to 100 ˚C

and 150 ˚C for 1 hour, respectively, followed by a final drying step at 200 ˚C for 2 hours. Afterward, the films were kept in a vacuum oven at 200 ˚C for 24 hours to further remove any residual solvent. The film was peeled off from the glass substrate by placing it in the DI water, then the film was dried at 70 ˚C in a vacuum oven. The thickness of PEI and its nanocomposites is in the range of 10-15 μm, measured by Heidenhain Length Gauges from Powertronics Incorporated. Gold electrodes with 6 mm diameter and thicknesses of 50 nm were sputtered on both sides of the PEI composites films for all the electrical measurements.

PEEU powder was synthesized by Key Synthesis LLC. To prepare the nanocomposite solution, a proper amount of PEEU powder was dissolved in dimethylformamide (DMF) at 60 ˚C and stirred overnight to obtain a homogeneous solution. Alumina nanoparticles (neat or modified) with selected volume content were dispersed in DMF at room temperature using an Elma "P" Series Ultrasonics (250 W) for 1 hour. Afterward, the PEEU solution was poured into this suspension and sonicated for 6 hours. Then, the solution was cast onto a Platinum (Pt) coated silicon plate and kept in a vacuum oven and dried at 80 ˚C for 12 hours to remove solvent. The obtained film was heated to 180 ˚C for 24 hours to further remove the solvent. The thickness of PEEU and its nanocomposites is in the range of 2-3 μm, measured by Profilometer (Tencor, P16). Pt electrodes of 4 mm diameter were sputtered on the composite films for the dielectric characterization.

IIC. Dielectric, X-ray diffraction, and SEM

Gold electrodes with 6 mm diameter and thicknesses of 50 nm were sputtered on both sides of the PEI composite films for all the electrical measurements. The dielectric constant was measured at 1kHz by a Hewlett-Packard (HP) 4284A LCR meter. The X-ray diffraction data for PEI nanocomposites were collected at room temperature using a Panalytical Xpert Pro MPD diffractometer. SEM (Scanning Electron Microscope) images were collected by Apreo 2 SEM.

Further experimental details of PEI and PEEU nanocomposites have been described in two earlier publications, Refs [16,17].

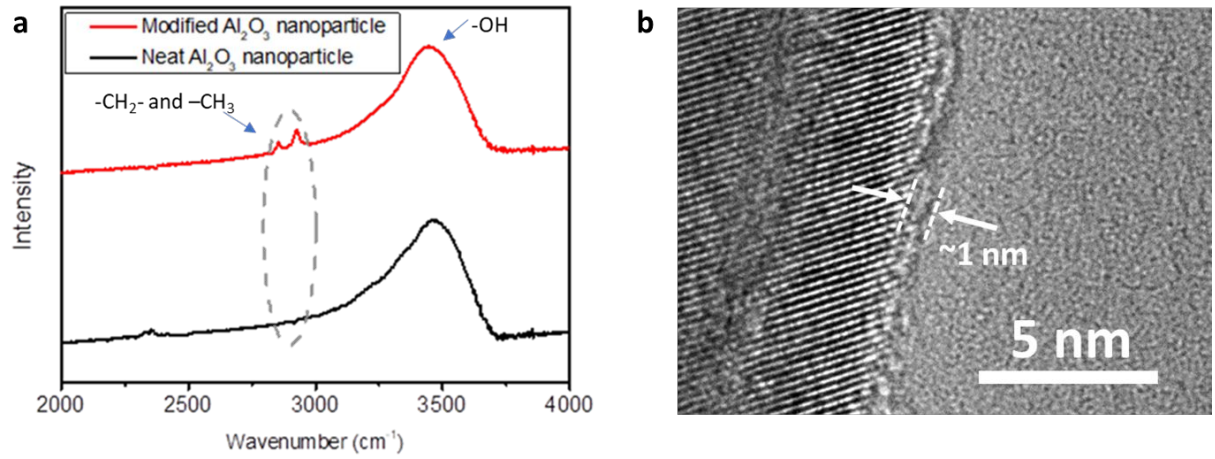

Fig. 1. (a) Infrared (IR) spectra and (b) Transmission electron microscopy (TEM) image of modified Alumina particles.

IID. Experimental results

In Fig. 1(a), the infrared spectra show that the modified particles still have the -OH groups as the original nanoparticles, but the modification also introduces alkyl groups that form a ~1nm thick coating on nanoparticles' surfaces, as shown in the TEM image, Fig. 1(b).

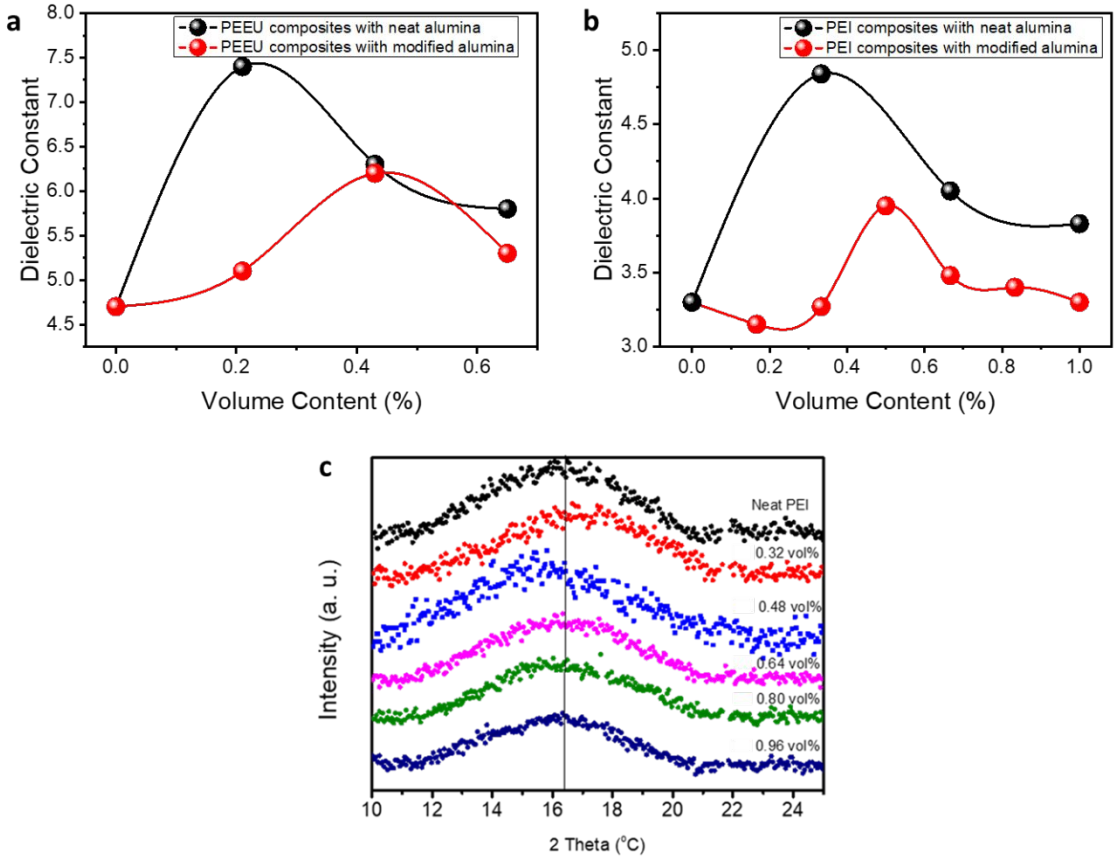

Fig. 2. (a)-(b) Dielectric constants of PEEU and PEI composites with 20 nm neat and modified Alumina nanoparticles versus nanoparticle volume content. (c) X-ray pattern of PEI nanocomposites with various volume content of modified Alumina particles.

Fig 2 compares the nanocomposites made with the modified nanoparticles versus those made with neat oxides. The peak dielectric constant decreased to 4.0 from 4.8 for the modified versus the neat PEI nanocomposite and to 6.2 from 7.4 for the PEEU nanocomposites. Furthermore, the peaks of the dielectric constant moved to higher volume% of the modified nanoparticles, indicating that the reduced propensity for hydrogen bond formation is partially compensated by an increase in the total surface area of nanoparticles, to which some chains can still attach. XRD data also shows that the broad amorphous peak for composites with 0.48 vol% modified nanoparticles is at a lower angle compared with other compositions.

III. COMPUTATIONAL MODEL AND METHODOLOGY

Based on the experimental observations, our model assumes that solvated polymers attach to the nanoparticles in solution. The polymer-nanoparticle bundles are then deposited on a surface and solidify into a film when the solvent evaporates. Obviously, this is a very complex, multistage process that is impossible to simulate in atomistic detail at present. Therefore, we simulate polymer chains that have already attached to nanoparticles and form a solid from condensed polymer-nanoparticle bundles. However, given the very low nanoparticle volume fraction, atomistic simulation of even a single polymer-nanoparticle bundle requires very large computational resources. Therefore, we develop a coarse-grained model that allows for studies of bundle formation, annealing, and coalescence. The coarse-grained potentials are developed from atomistic molecular dynamics (MD) simulations. Atomistic MD is then used to calculate the dipolar and the ionic parts of permittivity. The electronic part, due to the response of the electron cloud, is calculated by density functional theory calculations.

IIIA. Coarse-grained model

Considering the many hydroxy groups on oxide nanoparticle surfaces, the strongly-dipolar polymers with hydrogen-bond acceptors, such as PEEU, PEI, polyimide (PI), and polyaromatic ether ketone (PAEK), it is reasonable to assume that polymer chains attach to nanoparticles through hydrogen bonds. Therefore, in the coarse-grained simulations, the polymer-nanoparticle blob is modeled as a hairy "ball," i.e., the polymer chains saturate the nanoparticle's surface, which is taken as spherical for simplicity. A pristine polymer is modeled as parallel, densely packed chains.

The Kremer-Grest model is a widely used coarse-grained bead-spring model for studies of the morphologies of polymers. The original KG model includes a term accounting for the finite extensible nonlinear elastic (FENE) bonded interactions

$$U_{\mathrm{FENE}}(r) = \begin{cases} -\frac{kR^2}{2}\ln\left[1-\left(\frac{r}{R}\right)^2\right], \text{for } r < R \\ \infty, \qquad\qquad \text{for } r \geq R \end{cases} \tag{3}$$

and the Weeks-Chandler-Anderson (WCA) potential, i.e., a shifted and truncated repulsive 12-6 Lenard-Jones potential, for describing the nonbonded interactions

$$U_{\mathrm{WCA}}(r) = \begin{cases} 4\varepsilon\left[\left(\frac{\sigma}{r}\right)^{12} - \left(\frac{\sigma}{r}\right)^{6} + \frac{1}{4}\right], \text{for } r < 2^{\frac{1}{6}}\sigma \\ 0, \text{for } r \geqslant 2^{\frac{1}{6}}\sigma \end{cases} \tag{4}$$

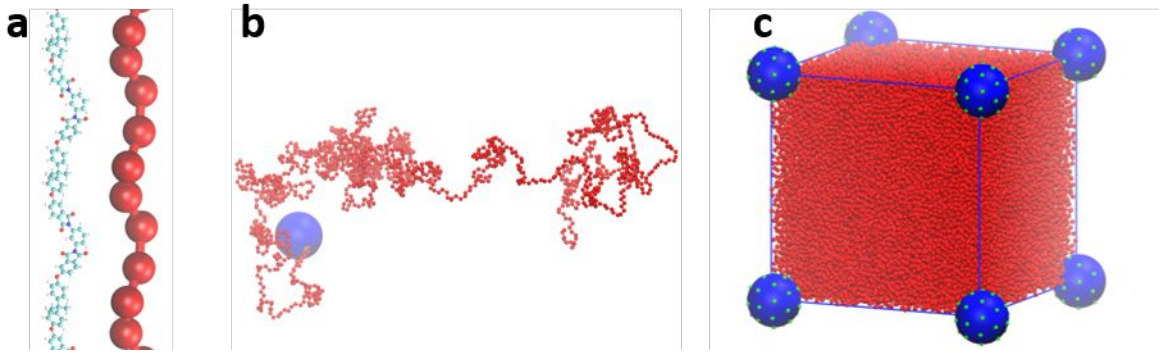

Fig. 3 (a) A PEI chain is coarse-grained into charged beads, (b) A coarse-grained polymer chain is grafted on a nanoparticle and is grown by self-avoiding random walk, (c) A periodic simulation box of a coarse-grained polymer nanocomposite with 32 chains grafted on each nanoparticle. Green dots mark the grafting sites.

We used a modified KG model, which includes bending-angle and torsional-angle interactions [23] and allows the beads to be charged [24]. The additional terms are:

$$U_{\text{bend}}(\theta) = \frac{k_\theta}{2}(\cos\theta - \cos\theta_0)^2 \tag{5}$$

where θ is the bending angle, and

$$U_{\text{torsion}}(\theta_1,\theta_2,\phi) = k_\phi \sin^3\theta_1 \sin^3\theta_2 \sum_{n=0}^{3} a_n \cos^n\phi \tag{6}$$

where ϕ is the torsional angle, and θ_1 and θ_2 are the bending angles.

For the nanocomposite simulations, the modified KG model was combined with a colloid potential to describe the interaction between polymer beads and the spherical nanoparticles. The form of this potential is [25]:

$$U_{\text{CS}}(r) = \frac{2R^3\sigma^3 A_{\text{CS}}}{9(R^2-r^2)^3}\left[1 - \frac{(5R^6 + 45R^4r^2 + 63R^2r^4 + 15r^6)\sigma^6}{15(R-r)^6(R+r)^6}\right], \text{for } r < r_{\text{c}} \tag{7}$$

The coarse-grained model reduces the number of particles by a factor of ~10, simplifies their interactions, and increases the timestep, speeding up the simulations by two orders of magnitude. A detailed list of parameters, developed from atomistic MD simulations, is given in Appendix A.

To study the morphology change of the polymers in nanocomposites, we perform molecular dynamics simulations using LAMMPS [26] with the coarse-grained parallel chains model for the pure polymers and the coarse-grained "hairy ball" model for polymer nanocomposites. For the parallel chains model, 32 polymer chains are initially aligned in parallel. For the nanocomposite simulations, 32 polymer chains were grafted onto the nanoparticle surface (the grafting sites were uniformly spaced) and "grown" by self-avoiding random walk addition of monomers until each chain was 2500 monomers long. The modeled systems were optimized through a simulated annealing procedure under zero pressure by (1) equilibration at temperature 0.3 ε/k_{B} for 100000

steps, (2) cooling down to 0.18 $\varepsilon/k_{\mathrm{B}}$ for 200000 steps, (3) equilibration at 0.18 $\varepsilon/k_{\mathrm{B}}$ for 100000 steps. For the optimized systems, the density profiles of the polymer nanocomposite and the pristine polymer systems were recorded.

IIIB. All-Atom Modeling and Molecular Dynamics

The all-atom molecular dynamics simulations were carried out using LAMMPS [26] with the ReaxFF force field. The ReaxFF is a bond-order-based force field originally designed to capture bond formation and bond breaking processes in chemical reactions. To achieve this, the force field is designed and parametrized to be as general as possible to model different chemical configurations formed by the same elements [27]. This is particularly useful for new polymers, for which optimized parametrizations do not yet exist. ReaxFF also includes a fluctuating charge model implemented through the electronegativity equalization method, which is essential to capturing the polarization response due to charge redistribution caused by atomic displacements [12]. The ReaxFF parameters were taken from Ref. [28] for PEEU and Ref. [22] for PEI.

The amorphous PEEU and PEI chains were modeled by 4 chains containing 1,832 and 1,112 atoms, corresponding to 48 monomers of PEEU and 16 monomers of PEI, respectively. The chains were aligned in parallel and placed in a periodic unit cell. To obtain the equilibrium densities, the cells were individually optimized through a simulated annealing procedure at zero pressure: (1) equilibration for 1 ns at 450 K, (2) cooling to 300 K at the rate of 250 K per ns, and (3) equilibration for 1 ns at 300 K. The temperature and pressure were controlled by the Nose-Hoover algorithm to generate the canonical (NVT) or isothermal-isobaric (NPT) ensembles [29,30]. The time step was 0.5 fs for all the simulations. To model polymers at lower densities, the unit cells at equilibrium were expanded uniformly in the two directions perpendicular to the polymer chains so that the densities were reduced to 85% of the equilibrium densities. After equilibration, the dipole moments were sampled at every time step for 1 ns to enable calculation of the vibrational contribution to permittivity.

The vibrational permittivity $K_s - K_\infty$ was calculated through the fluctuation formula [31,32]

$$K_s - K_\infty = \frac{4\pi\langle\vec{M}^2\rangle - \langle\vec{M}\rangle^2}{3 \quad k_B T V}, \tag{8}$$

where k_B is the Boltzmann constant, T is the thermodynamic temperature, V is the volume of the system, $\vec{M}$ is the total dipole moment, and $\langle\rangle$ is the averaging operation. The total dipole moment of a system is calculated as

$$\vec{M} = \sum_i q_i \vec{r}_i, \tag{9}$$

where q_i and $\vec{r}_i$ are the partial charge and position vector of ith particle, respectively, which are updated and recorded at each time step in our MD simulations. The dipole moment vary as the atomic positions change, accounting for the ionic and dipolar contributions to polarization, but not the electronic contributions. The complex dynamical permittivity is calculated using the fluctuation-dissipation theorem [32,33]

$$K(\omega) = K_s - \frac{4\pi}{3} \frac{i\omega}{k_B T V} \int_0^\infty e^{-i\omega t} \left(\langle \vec{M}_0 \cdot \vec{M}_t \rangle - \langle \vec{M} \rangle^2 \right) dt. \quad (10)$$

The imaginary part of $K(\omega)$ gives the dielectric loss $K'' = -Im(K)$. In this study, we fit the autocorrelation function of the dipole moment $\langle \vec{M}_0 \cdot \vec{M}_t \rangle - \langle \vec{M} \rangle^2$ to a multiexponential function to eliminate the noise from the molecular dynamics and the numerical Fourier-Laplace transform [34].

IIIC. Electronic Contribution to Permittivity

As shown in Refs. [12,14], the electronic permittivity is insensitive to the local morphology of polymers. Therefore, we use single-monomer unit cells to calculate the electronic permittivities by density functional perturbation theory (DFPT) [35].

Density functional theory (DFT) is used to optimize the unit cell and relax the atomic structure before DFPT is used to obtain the permittivity. DFPT calculates quantum mechanically the system's response due to a perturbation and obtains the dynamical matrix, phonons, Born effective charges, and the electronic permittivity. The DFPT computes the electronic permittivity using the formula

$$K^{\infty}_{\alpha\beta} = \delta_{\alpha\beta} - \frac{8\pi}{\Omega_0} \frac{\partial^2 E_{\text{el}}}{\partial \mathcal{E}^*_\alpha \partial \mathcal{E}_\beta}, \quad (11)$$

where $\delta_{\alpha\beta}$ is the Kronecker delta, Ω_0 is the volume of the unit cell, and $\frac{\partial^2 E_{\text{el}}}{\partial \mathcal{E}^*_\alpha \partial \mathcal{E}_\beta}$ is the mixed second-order derivative of the total energy with respect to the electric field. We calculate the scalar electronic permittivity as a simple cartesian average

$$K^{\infty} = \frac{K^{\infty}_{xx} + K^{\infty}_{yy} + K^{\infty}_{zz}}{3}. \quad (12)$$

DFPT obtains the total low-frequency permittivity using the formula

$$K_{\alpha\beta}(\omega) = K^{\infty}_{\alpha\beta} + \frac{4\pi}{\Omega_0} \sum_m \frac{S_{m,\alpha\beta}}{\omega_m^2 - \omega^2}, \quad (13)$$

where $S_{m,\alpha\beta}$ is the oscillator strength tensor for each zone-center optical phonon and ω_m is its frequency [36]. The static permittivity K_s is again obtained averaging the diagonal components at $\omega = 0$. The vibrational contribution to the permittivity is $K_s - K_\infty$.

The density functional theory and density functional perturbation theory calculations were carried out using the Quantum Espresso package [37], with the PBE exchange-correlation functional [38], and ultrasoft pseudopotentials [39]. The vdW-DF2 functional [40] was used to include van der Waals interactions between polymer chains. The energy cutoffs for wavefunctions and charge density were 60 Ry and 600 Ry, respectively. The convergence thresholds for the total energy, forces, and pressure were 0.0001 Ry, 0.001 Ry/bohr, and 3 bar, respectively. The target pressure was 0.

IV. COMPUTATIONAL RESULTS AND DISCUSSION

The results of coarse grain simulations are presented in Fig. 4. Setting the pure coarse-grained polymer's density at 1, the average density in the polymer nanocomposite is 0.85. The heat map of the density profile shows that the polymer nanocomposite has a quite uniform density distribution. Voids and free volume randomly appear not just near the nanoparticle's surface but also between the polymer chains.

We performed density functional perturbation theory calculations and molecular dynamics simulations on all-atom models of PEEU and PEI to connect the results of coarse-grained modeling to the observed permittivities. In DFPT calculations, the polymer “crystals” are represented by single-chain unit cells, containing 69 atoms for PEI and 38 atoms for PEEU. After geometry optimization using DFT, the vibrational and electronic permittivities were calculated using DFPT. In DFPT calculations for one monomer unit cells, the electronic permittivities are 2.98 for PEEU and 2.89 for PEI; while the static permittivities are 3.67 and 3.25, respectively. The vibrational permittivities are thus is 0.69 for PEEU and 0.36 for PEI.

To assess the ReaxFF interatomic potentials' quality, we carried out molecular dynamics for the same “crystals”. The resulting vibrational permittivities were 0.71 for PEEU and 0.33 for PEI, consistent with the DFPT calculations. The results for both sets of calculations are summarized in Table 1.

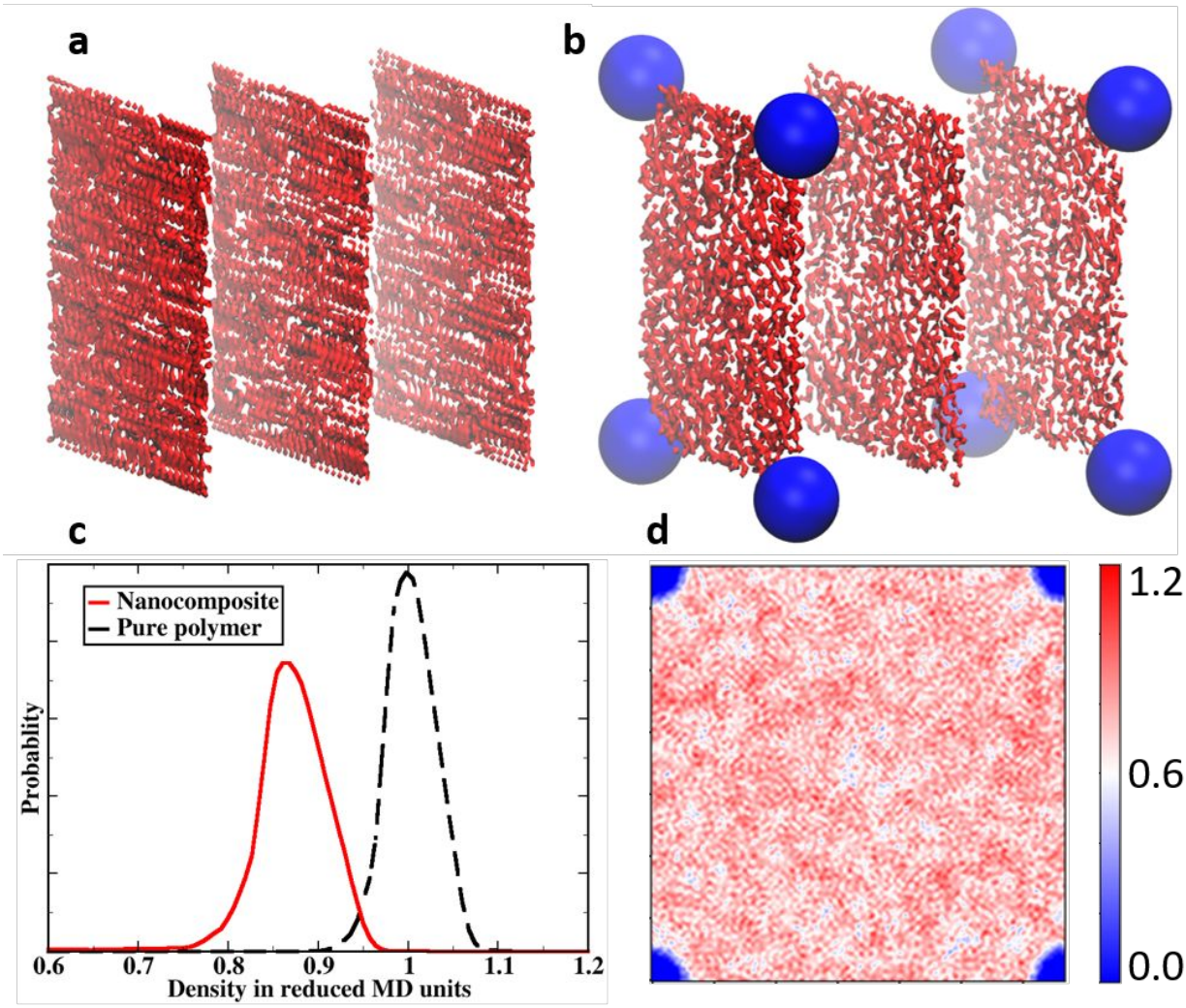

Fig. 4. Results of coarse-grained MD simulations of pure polymers and nanocomposites: (a) Slices of pure polymer cell show well-packed polymer chains with little free volume, (b) Slices of polymer-nanoparticle composite with significantly more free volume, (c) Polymer density distributions of the nanocomposite and the pure polymer, (d) Polymer density distribution heatmap in a planar slice of the simulated nanocomposite. The nanoparticles are located at the corners where the polymer density is zero (colored in blue). The color map highlights the regions of high and low densities.

Table 1 Vibrational permittivities of polymer "crystals"

	$K_s - K_\infty$ from MD/ReaxFF	$K_s - K_\infty$ from DFPT
PEEU “crystal”	0.71	0.69 (K_∞=2.98)
PEI “crystal”	0.33	0.36 (K_∞=2.89)

We now turn to large-scale molecular dynamics calculations. In the MD simulations of amorphous polymers, we used 4 chains with 12 monomers each for PEEU and 4 monomers each for PEI. After annealing and equilibration, the chains are partially twisted and disordered, resulting in effectively amorphous structures. The equilibrium density at zero pressure for PEEU is 1.49 g/cm^3, with a vibrational permittivity of 1.77. For PEI, the equilibrium density is 1.45 g/cm^3, with the vibrational permittivity of 0.46. At 85% of their original densities (1.26 g/cm^3 for PEEU and 1.21 g/cm^3 for PEI), the vibrational permittivities become 4.63 for PEEU and 2.54 for PEI. The permittivities are thus increased by 2.86 for PEEU and by 2.08 for PEI. The calculated data are listed in Table 2.

Table 2 Calculated permittivities of amorphous polymers

	$K_s - K_\infty$	K_s
1.49 g/cm^3 PEEU amorphous	1.77	4.75
1.26 g/cm^3 PEEU amorphous	4.63	7.61
1.45 g/cm^3 PEI amorphous	0.46	3.35
1.21 g/cm^3 PEI amorphous	2.54	5.43

We also calculated the dielectric loss, eq. 10, and use it to analyze the dielectric enhancement. The dielectric loss spectra (Fig. 5), show that the low-frequency modes are enhanced in low-densities PEEU and PEI, compared to those at their equilibrium densities. Compared to pure PEEU with the density of 1.49 g/cm^3, the PEEU with the density of 1.26 g/cm^3 has more intensive peaks around ~100 GHz, while the PEI with the density of 1.21 g/cm^3 has more intensive peaks around ~10 and ~100 GHz than the pure PEI with the density of 1.45 g/cm^3. This indicates that more low-frequency modes are activated with increased free volume and that the low-frequency dielectric response is enhanced. The real and imaginary parts of the frequency-dependent dielectric constant (Fig. 5) also show that the increase of dielectric constant come from the contributions of low frequency modes, where the peaks of the dielectric loss reside. This can be understood from Eq. 13: with the squared frequency singular terms in the denominator, low-frequency newly activated vibrational modes contribute more to the low-frequency dielectric constant.

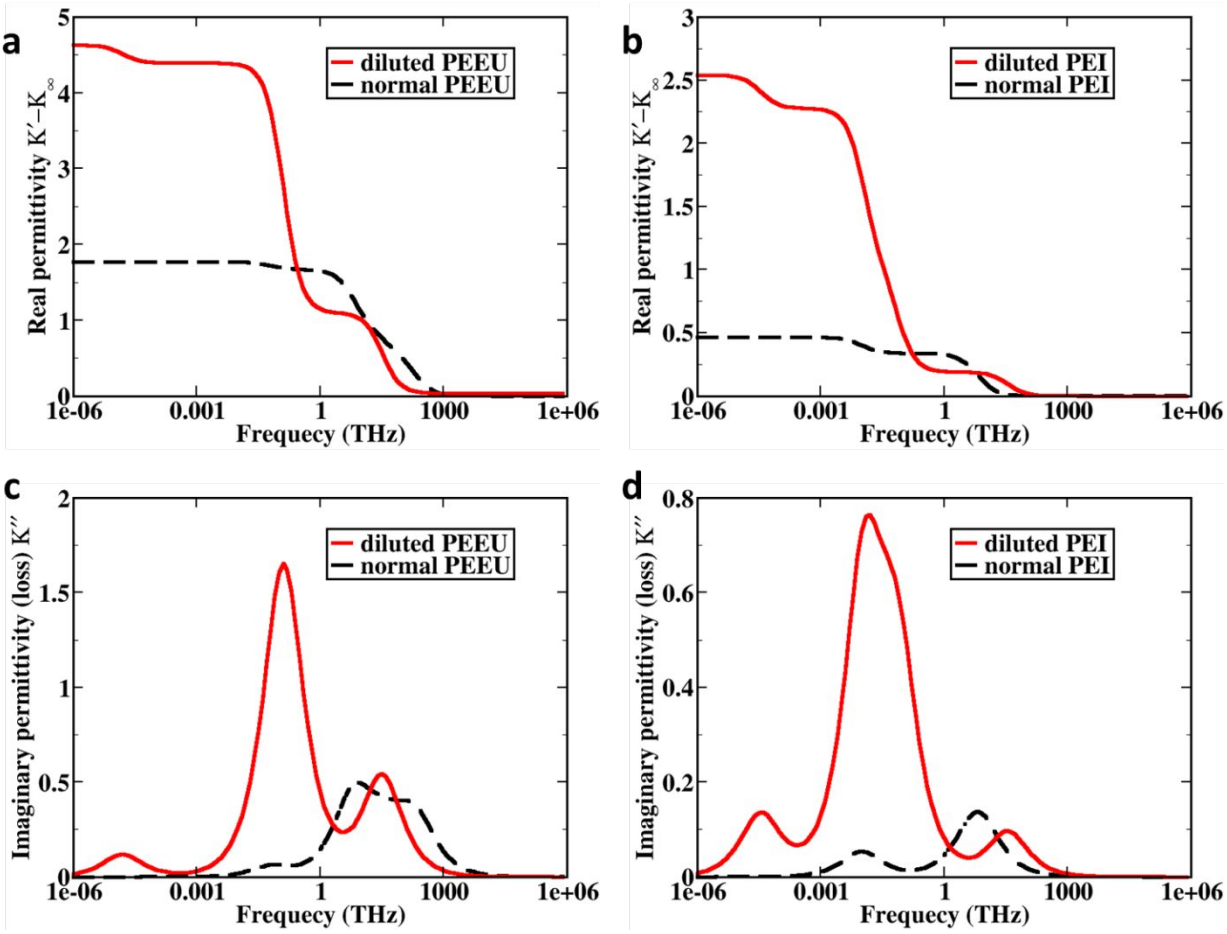

Fig. 5. Calculated atomic-motion parts of complex permittivities for PEEU and PEI at 85% of equilibrium and normal (100%) densities: (a)(c) the real and imaginary parts of atomic-motion contributions to complex dielectric constant for PEEU; (b)(d) the real and imaginary parts of atomic-motion contributions to complex dielectric constant for PEI.

The calculated enhancement due to increased free volume is in qualitative agreement with a recent computational study of PEI chains attached to an Al_2O_3 surface [22]. This study showed that the dielectric constant is significantly increased at distances between 2 and 6 nm from the surface, reaching a value of 20 at 4 nm. However, a 2 nm thin shell of enhanced permittivity around each nanoparticle is not sufficient to reach the observed 56% enhancement at particle concentrations smaller than 1 vol%.

In contrast, our nucleation-aggregation model of nanoparticle-polymer beads leads to reduced polymer density in the entire film, as shown by the coarse-grained simulations. The increased free volume throughout the film increases its dielectric permittivity, in very good agreement with the experimental data. For PEEU, the calculated value of nanocomposite permittivity is 7.6 (Table 3), while the experimental value is 7.4 [17]. For PEI, we obtain 5.4, compared to the measured result of 5.0 [16]. However, since our simulation times are ~ 1 ns, the sub-GHz frequencies are not accessible. This may explain why the calculated dielectric enhancement is lower than the empirical model's prediction [16], in addition to the approximations inherent in coarse-grained modeling of film morphology.

V. SUMMARY AND CONCLUSIONS

This work has investigated permittivity enhancement in dilute polymer nanocomposites, which are formed by adding less than 1 vol% of nanometer size particles to polymer solution, before solution casting of the dielectric film. Our experiments show that by weakening the hydrogen-bond interaction between the nanoparticles and the polymer, the dielectric constant enhancement is reduced. Accordingly, our computational model assumes that polymers attach to the nanoparticles via hydrogen bonds in solution, followed by deposition of nanoparticle-polymer blobs during solution casting. Blob formation and aggregation were modeled using coarse-grained simulations. The coarse-graining involved constructing simplified polymer potentials of a modified Kremer-Grest form from atomistic calculations, followed by nanocomposite morphology simulations. The monomer density in the polymer nanocomposite turned out to be 15% lower than that of a pure polymer. This is mainly caused by the constraints on the nanoparticle's surface where the polymer chains are anchored, preventing them from fully extending to fill the space. The large increase of the free volume in the nanocomposite enables easier reorientation and alignment of polymer dipoles with the field, leading to an enhancement of the dielectric constant.

The electronic parts of the dielectric constants, which are largely structure insensitive, were calculated using density functional theory, while the vibrational parts for purely crystalline polymers were obtained via both DFT and all-atom molecular dynamics with the ReaxFF force field. The vibrational parts evaluated by the two methods were in close agreement with each other, confirming the accuracy of the ReaxFF force field for calculating dielectric properties. All-atom MD simulations were then performed for amorphous PEEU and PEI polymers, both at their equilibrium densities and at 85% of these densities. The results at equilibrium densities agree well with the experimental data for pristine polymer films, while those for low-density polymers are in very good agreement with the experimental results for nanocomposites. The anticipated origin of the enhancement was confirmed by analyzing the imaginary part of the complex permittivity. We found that the low-frequency response between 10 and 100 GHz is enlarged in polymer nanocomposites compared to the pristine polymers, consistent with the intuitive understanding of the effects of enhanced free volume.

Conflicts of interest

There are no conflicts of interest to declare.

Acknowledgments

This research was supported by the U. S. ONR, grant number N00014-19-1-2033 (NC State) and N00014-19-1-2028 (Penn State). The calculations were performed at Oak Ridge Leadership Computing Facility, supported by DOE contract DE-AC05-00OR22725.

Appendix A.

Table A1 Parameters in coarse-grained simulations *[23]*.

Parameter	In MD units

ϵ in WCA potential and LJ potential	1
σ in WCA potential and LJ potential	1
k in FENE potential	30
R in FENE potential	1.5
k_θ in bending potential	25
$\cos\theta_0$ in bending potential	-0.333
k_ϕ in torsional potential	1
a_0 in torsional potential	3.0
a_1 in torsional potential	-5.9
a_2 in torsional potential	2.06
a_3 in torsional potential	10.9

Table A2 dielectric constant summary for PEI composites with 20 nm Alumina particles

Sample #	1	2	3	4	5
0 vol%	3.20	3.23	3.22	3.19	3.17
0.32 vol%	4.81	5.01	5.33	4.67	4.43
0.64 vol%	4.38	3.91	3.84	4.21	4.05
0.96 vol%	3.79	3.84	3.78	3.87	3.98

Table A3 dielectric constant summary for PEI composites with modified 20 nm Alumina particles

Sample #	1	2	3
0.16 vol%	3.14	3.11	3.16
0.32 vol%	3.18	3.27	3.27
0.48 vol%	4.11	3.69	3.95
0.64 vol%	3.48	3.44	3.37
0.80 vol%	3.39	3.43	3.39
0.96 vol%	3.28	3.29	3.30

References

[1] T. Christen, M.W. Carlen, Theory of Ragone plots, J. Power Sources. 91 (2000) 210–216. https://doi.org/10.1016/S0378-7753(00)00474-2.

[2] M. Rabuffi, G. Picci, Status quo and future prospects for metallized polypropylene energy storage capacitors, IEEE Trans. Plasma Sci. 30 (2002) 1939–1942.

[3] Q. Chen, Y. Shen, S. Zhang, Q.M. Zhang, Polymer-based dielectrics with high energy storage density, Annu. Rev. Mater. Res. 45 (2015) 433–458.

[4] B. Chu, X. Zhou, K. Ren, B. Neese, M. Lin, Q. Wang, F. Bauer, Q.M. Zhang, A dielectric polymer with high electric energy density and fast discharge speed, Science. 313 (2006) 334–336.

[5] V. Ranjan, L. Yu, M.B. Nardelli, J. Bernholc, Phase equilibria in high energy density PVDF-based polymers, Phys. Rev. Lett. 99 (2007) 047801.

[6] B. Neese, B. Chu, S.-G. Lu, Y. Wang, E. Furman, Q.M. Zhang, Large electrocaloric effect in ferroelectric polymers near room temperature, Science. 321 (2008) 821–823.

[7] V. Ranjan, M.B. Nardelli, J. Bernholc, Electric field induced phase transitions in polymers: a novel mechanism for high speed energy storage, Phys. Rev. Lett. 108 (2012) 087802.

[8] P. Kim, S.C. Jones, P.J. Hotchkiss, J.N. Haddock, B. Kippelen, S.R. Marder, J.W. Perry, Phosphonic acid-modified barium titanate polymer nanocomposites with high permittivity and dielectric strength, Adv. Mater. 19 (2007) 1001–1005.

[9] Y. Wang, L. Wang, Q. Yuan, Y. Niu, J. Chen, Q. Wang, H. Wang, Ultrahigh electric displacement and energy density in gradient layer-structured BaTiO 3/PVDF nanocomposites with an interfacial barrier effect, J. Mater. Chem. A. 5 (2017) 10849–10855.

[10] S. Wu, Q. Burlingame, Z.-X. Cheng, M. Lin, Q.M. Zhang, Strongly dipolar polythiourea and polyurea dielectrics with high electrical breakdown, low loss, and high electrical energy density, J. Electron. Mater. 43 (2014) 4548–4551.

[11] Y. Thakur, R. Dong, M. Lin, S. Wu, Z. Cheng, Y. Hou, J. Bernholc, Q.M. Zhang, Optimizing nanostructure to achieve high dielectric response with low loss in strongly dipolar polymers, Nano Energy. 16 (2015) 227–234.

[12] R. Dong, V. Ranjan, M.B. Nardelli, J. Bernholc, Atomistic simulations of aromatic polyurea and polyamide for capacitive energy storage, Phys. Rev. B. 92 (2015) 024203.

[13] Y. Thakur, M. Lin, S. Wu, Q.M. Zhang, Aromatic Polyurea Possessing High Electrical Energy Density and Low Loss, J. Electron. Mater. 45 (2016) 4721–4725.

[14] Y. Thakur, B. Zhang, R. Dong, W. Lu, C. Iacob, J. Runt, J. Bernholc, Q.M. Zhang, Generating high dielectric constant blends from lower dielectric constant dipolar polymers using nanostructure engineering, Nano Energy. 32 (2017) 73–79.

[15] V. Sharma, C. Wang, R.G. Lorenzini, R. Ma, Q. Zhu, D.W. Sinkovits, G. Pilania, A.R. Oganov, S. Kumar, G.A. Sotzing, Rational design of all organic polymer dielectrics, Nat. Commun. 5 (2014) 1–8.

[16] Y. Thakur, T. Zhang, C. Iacob, T. Yang, J. Bernholc, L.Q. Chen, J. Runt, Q.M. Zhang, Enhancement of the dielectric response in polymer nanocomposites with low dielectric constant fillers, Nanoscale. 9 (2017) 10992–10997.

[17] T. Zhang, X. Chen, Y. Thakur, B. Lu, Q. Zhang, J. Runt, Q.M. Zhang, A highly scalable dielectric metamaterial with superior capacitor performance over a broad temperature, Sci. Adv. 6 (2020) eaax6622.

[18] B. Wen, M. Cao, M. Lu, W. Cao, H. Shi, J. Liu, X. Wang, H. Jin, X. Fang, W. Wang, Reduced graphene oxides: light-weight and high-efficiency electromagnetic interference shielding at elevated temperatures, Adv. Mater. 26 (2014) 3484–3489.
[19] M. Cao, X. Wang, W. Cao, X. Fang, B. Wen, J. Yuan, Thermally driven transport and relaxation switching self-powered electromagnetic energy conversion, Small. 14 (2018) 1800987.
[20] Y.-H. Jia, P. Gong, S.-L. Li, W.-D. Ma, X.-Y. Fang, Y.-Y. Yang, M.-S. Cao, Effects of hydroxyl groups and hydrogen passivation on the structure, electrical and optical properties of silicon carbide nanowires, Phys. Lett. A. 384 (2020) 126106.
[21] Y.-J. Li, S.-L. Li, P. Gong, Y.-L. Li, X.-Y. Fang, Y.-H. Jia, M.-S. Cao, Effect of surface dangling bonds on transport properties of phosphorous doped SiC nanowires, Phys. E Low-Dimens. Syst. Nanostructures. 104 (2018) 247–253.
[22] C.U. Gonzalez-Valle, S.H. Hahn, M.G. Muraleedharan, Q. Zhang, A.C. van Duin, B. Ramos-Alvarado, Investigation into the Atomistic Scale Mechanisms Responsible for the Enhanced Dielectric Response in the Interfacial Region of Polymer Nanocomposites, J. Phys. Chem. C. (2020).
[23] M. Bulacu, E. van der Giessen, Molecular-dynamics simulation study of the glass transition in amorphous polymers with controlled chain stiffness, Phys. Rev. E. 76 (2007) 011807.
[24] U. Micka, K. Kremer, Strongly charged flexible polyelectrolytes in poor solvents—from stable spheres to necklace chains, EPL Europhys. Lett. 49 (2000) 189.
[25] J. Kalb, D. Dukes, S.K. Kumar, R.S. Hoy, G.S. Grest, End grafted polymer nanoparticles in a polymeric matrix: Effect of coverage and curvature, Soft Matter. 7 (2011) 1418–1425.
[26] S. Plimpton, Fast Parallel Algorithms for Short-Range Molecular Dynamics, J. Comput. Phys. 1 (1995) 1–19. https://doi.org/10.1006/jcph.1995.1039.
[27] A.C. Van Duin, S. Dasgupta, F. Lorant, W.A. Goddard, ReaxFF: a reactive force field for hydrocarbons, J. Phys. Chem. A. 105 (2001) 9396–9409.
[28] T.R. Mattsson, J.M.D. Lane, K.R. Cochrane, M.P. Desjarlais, A.P. Thompson, F. Pierce, G.S. Grest, First-principles and classical molecular dynamics simulation of shocked polymers, Phys. Rev. B. 81 (2010) 054103.
[29] G.J. Martyna, M.L. Klein, M. Tuckerman, Nosé–Hoover chains: The canonical ensemble via continuous dynamics, J. Chem. Phys. 97 (1992) 2635–2643.
[30] G.J. Martyna, D.J. Tobias, M.L. Klein, Constant pressure molecular dynamics algorithms, J. Chem. Phys. 101 (1994) 4177–4189.
[31] M. Neumann, Dipole moment fluctuation formulas in computer simulations of polar systems, Mol. Phys. 50 (1983) 841–858.
[32] N. Karasawa, W.A. Goddard III, Dielectric properties of poly (vinylidene fluoride) from molecular dynamics simulations, Macromolecules. 28 (1995) 6765–6772.
[33] R. Kubo, The fluctuation-dissipation theorem, Rep. Prog. Phys. 29 (1966) 255.
[34] C. Schröder, O. Steinhauser, Using fit functions in computational dielectric spectroscopy, J. Chem. Phys. 132 (2010) 244109.
[35] S. Baroni, S. De Gironcoli, A. Dal Corso, P. Giannozzi, Phonons and related crystal properties from density-functional perturbation theory, Rev. Mod. Phys. 73 (2001) 515.
[36] X. Gonze, C. Lee, Dynamical matrices, Born effective charges, dielectric permittivity tensors, and interatomic force constants from density-functional perturbation theory, Phys. Rev. B. 55 (1997) 10355.

[37] P. Giannozzi, S. Baroni, N. Bonini, M. Calandra, R. Car, C. Cavazzoni, D. Ceresoli, G.L. Chiarotti, M. Cococcioni, I. Dabo, QUANTUM ESPRESSO: a modular and open-source software project for quantum simulations of materials, J. Phys. Condens. Matter. 21 (2009) 395502.
[38] J.P. Perdew, K. Burke, M. Ernzerhof, Generalized gradient approximation made simple, Phys. Rev. Lett. 77 (1996) 3865.
[39] D. Vanderbilt, Soft self-consistent pseudopotentials in a generalized eigenvalue formalism, Phys. Rev. B. 41 (1990) 7892.
[40] K. Lee, É.D. Murray, L. Kong, B.I. Lundqvist, D.C. Langreth, Higher-accuracy van der Waals density functional, Phys. Rev. B. 82 (2010) 081101.